


# Development of an Intelligent Reactive Oxygen Species-Responsive Dual-Drug Delivery Nanoplatfrom for Enhanced Precise Therapy of Acute Lung Injury

Dunling Xia<sup>1</sup>, Zongqing Lu<sup>1</sup>, Shuai Li<sup>1</sup>, Pu Fang<sup>1</sup>, Chun Yang<sup>2</sup>, Xiaoyan He<sup>3</sup>, Qinghai You<sup>1</sup>, Gengyun Sun<sup>1</sup> 

<sup>1</sup>Department of Respiratory and Critical Care Medicine, the First Affiliated Hospital of Anhui Medical University, Hefei, People's Republic of China;

<sup>2</sup>Department of Emergency Intensive Care Unit, the First Affiliated Hospital of Anhui Medical University, Hefei, People's Republic of China; <sup>3</sup>School of Life Sciences, Anhui Medical University, Hefei, People's Republic of China

Correspondence: Qinghai You; Gengyun Sun, Department of Respiratory and Critical Care Medicine, the First Affiliated Hospital of Anhui Medical University, 218 Jixi Road, Sanli'an Street, Shushan District, Hefei, Anhui Province, 230032, People's Republic of China, Tel +86 551 6292 2913, Fax +86 551 6292 2752, Email amormor@126.com; sungengy@126.com

**Introduction:** Acute lung injury (ALI) and its most severe form acute respiratory distress syndrome (ARDS) are commonly occurring devastating conditions that seriously threaten the respiratory system in critically ill patients. The current treatments improve oxygenation in patients with ALI/ARDS in the short term, but do not relieve the clinical mortality of patients with ARDS.

**Purpose:** To develop the novel drug delivery systems that can enhance the therapeutic efficacy of ALI/ARDS and impede adverse effects of drugs.

**Methods:** Based on the key pathophysiological process of ARDS that is the disruption of the pulmonary endothelial barrier, bilirubin (Br) and atorvastatin (As) were encapsulated into an intelligent reactive oxygen species (ROS)-responsive nanocarrier DSPE-TK-PEG (DPTP) to form nanoparticles (BA@DPTP) in which the thioketal bonds could be triggered by high ROS levels in the ALI tissues.

**Results:** BA@DPTP could accumulate in inflammatory pulmonary sites through passive targeting strategy and intelligently release Br and As only in the inflammatory tissue via ROS-responsive bond, thereby enhancing the drugs effectiveness and markedly reducing side effects. BA@DPTP effectively inhibited NF- $\kappa$ B signaling and NLRP3/caspase-1/GSDMD-dependent pyroptosis in mouse pulmonary microvascular endothelial cells. BA@DPTP not only protected mice with lipopolysaccharide-induced ALI and retained the integrity of the pulmonary structure, but also reduced ALI-related mortality.

**Conclusion:** This study combined existing drugs with nano-targeting strategies to develop a novel drug-targeting platform for the efficient treatment of ALI/ARDS.

**Keywords:** acute lung injury, acute respiratory distress syndrome, reactive oxygen species-responsiveness, nanoparticles, bilirubin, atorvastatin

## Introduction

Both acute lung injury (ALI) and the more severe form acute respiratory distress syndrome (ARDS) are serious illnesses that commonly affect the respiratory system of critically ill patients.<sup>1</sup> The mortality rate of patients with severe ARDS is as high as 45%, which places a tremendous burden on the global healthcare system.<sup>2,3</sup> History has repeatedly shown that pathogens can cause catastrophic damage to the human respiratory system. Many respiratory viruses could cause severe runaway immune-mediated ROS damage, such as Severe Acute Respiratory Syndrome and Middle East Respiratory Syndrome can cause ALI/ARDS.<sup>4,5</sup> The severe acute respiratory syndrome coronavirus 2, responsible for the recent Coronavirus disease 2019 (COVID-19) pandemic, is also an example. According to the report by the World Health Organization, the current confirmed global

COVID-19-related deaths due to acute respiratory failure have exceeded 7 million.<sup>6,7</sup> Because of the unique physiological barriers of the lung, pulmonary drug delivery to inflamed tissues is relatively inefficient, resulting in decreased drug therapeutic effectiveness and enhanced systemic side effects.<sup>8</sup> Therefore, the development of novel drug delivery systems that can enhance the therapeutic efficacy and impede adverse effects of drugs is urgent for successful ALI/ARDS therapy.

The most common inducement for ALI/ARDS is lung infection. A key underlying pathogenic mechanism is the breakdown of the lung endothelial barrier function due to widespread endothelial cell death and disassembly of endothelial adherens junctions, which can lead to protein-rich non-hydrostatic pulmonary edema, lung stiffness, reduced lung volume, refractory hypoxemia and impairment of lung function in eliminating carbon dioxide.<sup>9–11</sup> The endothelium is distributed throughout the entire vascular system, especially the lung endothelium, which accounts for approximately 50% of all lung cells and receives the total right cardiac output.<sup>12</sup> The complete endothelial barrier strictly controls pulmonary vascular permeability and leukocyte recruitment, whereas a broken endothelial barrier is eventually responsible for severe ARDS and the associated high mortality rates.<sup>13,14</sup> Furthermore, previous studies have revealed that oxidative stress, pyroptosis, and excessive release of proinflammatory cytokines are also features of the pathological process of ARDS.<sup>12,15–18</sup>

The current treatments for ARDS mainly include extracorporeal membrane oxygenation (ECMO), mechanical ventilation, nutritional support, strict fluid management, and other symptomatic supportive therapy. Although those measures improve oxygenation in patients in the short term, they still do not mitigate the clinical mortality rates of patients with ARDS.<sup>19</sup> Moreover, the use of ECMO or ventilators may cause a secondary hit that exacerbates lung injury.<sup>10,20</sup> In addition, there is a serious shortage of ECMO and ventilator equipment as well as medical staff during fatal epidemic bursts. A large number of drug candidates for ARDS has been reported in recent years; unfortunately, none of them have been proven to be effective in reducing mortality in clinical trials.<sup>7</sup> This may be attributed to the heterogeneity in patients with ARDS and the unique physiological barriers of the lung, in which complexity pathophysiologic mechanism reduces the efficiency of drug delivery to the injured lung tissues, leading to unfavorable outcomes and side effects.<sup>8</sup>

In this study, bilirubin (Br) and atorvastatin (As) were used to synergistically treat ARDS based on the pathophysiological process. Br is an ingredient in Ningxin Pill, a commonly used drug in clinics.<sup>21</sup> Previous studies have shown that Br possesses a strong ability to resist oxidative stress.<sup>22,23</sup> The efficiency of statins against ARDS is known: in comparison to the effects of a placebo, it has been verified to improve 28- and 90-day survival in a randomized double-blind prospective trial.<sup>24</sup> Unconjugated bilirubin presents crucial therapeutic effects of anti-inflammation and antioxidants for protecting cells and tissues. However, they can also cause irreversible damage to the brain and nervous system due to excessive Br aggregates in various tissues, a condition known as jaundice,<sup>25</sup> which limits the clinical application of Br.

In ALI, there is also increased production of reactive oxygen species (ROS) in inflammatory tissues,<sup>26,27</sup> which offers a target for accurate drug release to lung inflammatory tissues. Herein, our study devised a ROS-responsive nanocarrier to achieve the intelligent release of drugs to lung inflammatory tissues for enhanced precise therapy of ALI. Br and As were simultaneously encapsulated in the nanocarrier involving a thioketal bond to obtain the ROS-responsive nanoparticles (NPs) named BA@DPTP. The two longstanding oral drugs Br and As were transformed into an innovative targeted nanomedicine, providing a novel candidate for effective drug therapy for ALI/ARDS. Furthermore, we investigated the mechanisms of BA@DPTP's therapeutic effects *ex vivo*. The loaded Br and As are expected to release in response to a high ROS environment in the lung tissue of ALI, effectively suppressing the inflammation, retaining the integrity of the pulmonary structure, and reducing the mortality rates associated with ALI (Figure 1).

## Materials and Methods

### Chemicals

1,2-stearoyl-sn-glycerol-3-phosphoethanolamine (DSPE), trichloromethane, methoxy(polyethyleneglycol)-2000 (MPEG), N1-((methylamino)methylene)-N3,N3-dimethyl propane-1,3-diamine (EDC), 4-dimethylamino pyridine (DMAP), (2-dimethylamino propyl)-N-ethyl carbodiimide, dichloromethane, acetonitrile, Nile red, and Cyanine 5.5 (CY5.5) were provided by J&K Scientific (Beijing, China). Bilirubin (Br), atorvastatin (As), Lipopolysaccharide (LPS) from *Escherichia coli*, O111:B4, Evans blue (EB), and fluorescein isothiocyanate (FITC)-dextran were purchased from Sigma-Aldrich (St. Louis, USA). Dulbecco's modified Eagle medium (DMEM) and phosphate-buffered saline (PBS) were purchased from

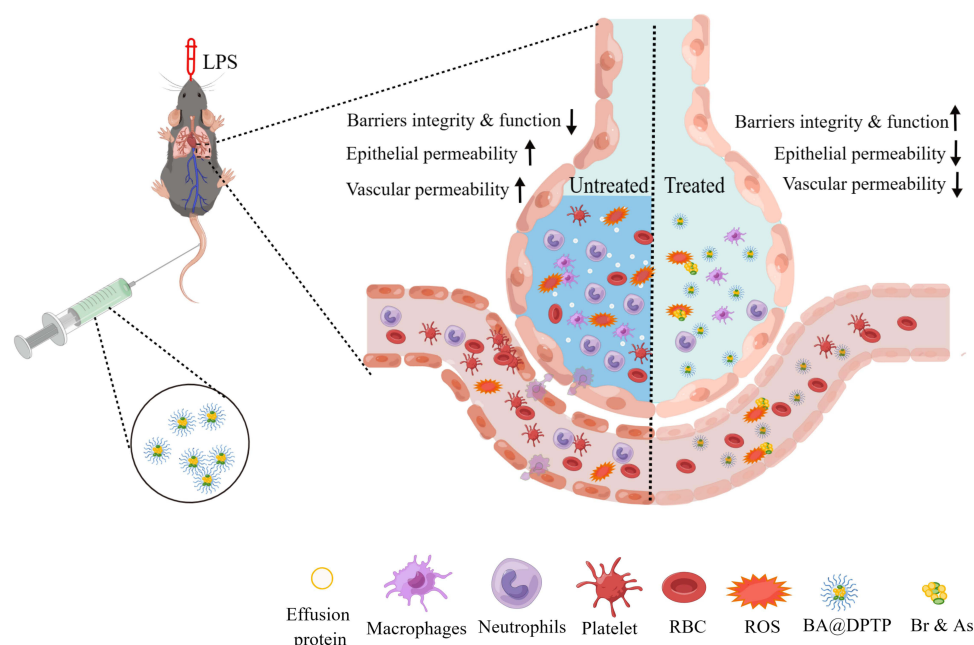


**Figure 1** The scheme of the LPS-induced ALI model with intratracheally administered LPS (10 mg/kg). Scheme to show the in vivo therapy of ALI by using BA@DPTP. The intravenously injected BA@DPTP accumulate in lung, and release drugs triggered by the high level of ROS, resulting in decreased immune cell infiltration, a lower level of cytokines and thereby reduced lung injury.

HyClone (Logan, USA). Cell counting kit 8 was provided by Dojindo (Tokyo, Japan). Lactate dehydrogenase (LDH) cytotoxicity assay kit was provided by Promega (Madison, USA). Penicillin/streptomycin (P/S), phenylmethyl sulfonyl fluoride (PMSF), ROS assay kit, PI staining kit, BCA Protein Assay Kit, and 4'-6-diamidino-2-phenylindole (DAPI) were obtained from Beyotime Biotechnology (Shanghai, China). Fetal bovine serum (FBS) and endothelial cell-derived growth factor (ECGS) were provided by ScienCell (Carlsbad, USA). Bovine serum albumin (BSA) was purchased by Aladdin Chemistry Co., Ltd. (China). Enzyme-linked immunosorbent assay (ELISA) kit for interleukin-1 $\beta$  (IL-1 $\beta$ ), interleukin-18 (IL-18), and tumor necrosis factor- $\alpha$  (TNF- $\alpha$ ) were obtained from Multisciences Biotech (China). Antibodies against P65 and p-P65 were purchased from Cell Signaling Technology (Beverly, MA, USA). Antibodies against NLRP3, caspase 1, and GSDMD were purchased from Abcam (Britain). Antibodies against GAPDH, horseradish peroxidase (HRP)-conjugated anti-rabbit IgG, and Alexa Fluor 488-conjugated secondary antibodies and were purchased from Proteintech (China). The syringe filter (0.22  $\mu$ m) was purchased from Millipore (Billerica, MA, USA).

## Preparation and Characterization of Nanoparticles (NPs)

DSPE-NH<sub>2</sub> (100 mg), MPEG2K-TK-COOH (1.0 eq.), EDC (2.0 eq.), and DMAP (0.5 eq.) were dissolved in 3 mL of chloroform (CHCl<sub>3</sub>), and the reaction was performed at 40°C for 4 h with stirring. Then, the reaction mixture was concentrated via vacuum rotary evaporation. Afterward, the 4°C ethyl ether was added to precipitate the excess impurities. Finally, DSPE-TK-PEG (DPTP) was obtained after freeze-drying. Fortunately, BA@DPTP nanoparticles were successfully synthesized as shown in Figure 2. To prepare the dual-load NPs (BA@DPTP), the Br (6mg) and AS (3mg) were dissolved in dichloromethane (1mL) and the DPTP (20mg) was dissolved in ultrapure water (1mL). Secondly, the dual-drug solution and the aqueous solution of DPTP were mixed. Next, the mixture was gradually added to ultrapure water (5mL) under the ultrasonic state at room temperature until the mixed solution was translucent. Immediately the mixture was dialyzed by using a polycarbonate membrane (pore size 50 nm) for 24 h to remove the unloaded Br and As completely. Afterward, the resulting emulsions were magnetically stirred in a water bath (41°C) for 6 h to completely evaporate dichloromethane. Finally, the NPs were obtained by centrifugation for 10 min at 12,000 g and washed with ultrapure water for 3 times. The NPs were re-dissolved in ultrapure water and kept at 4°C before use. The Br-loaded NPs (BR@DPTP) and As-loaded NPs (AS@DPTP) were obtained by using the same procedure. Cy5.5 or Nile

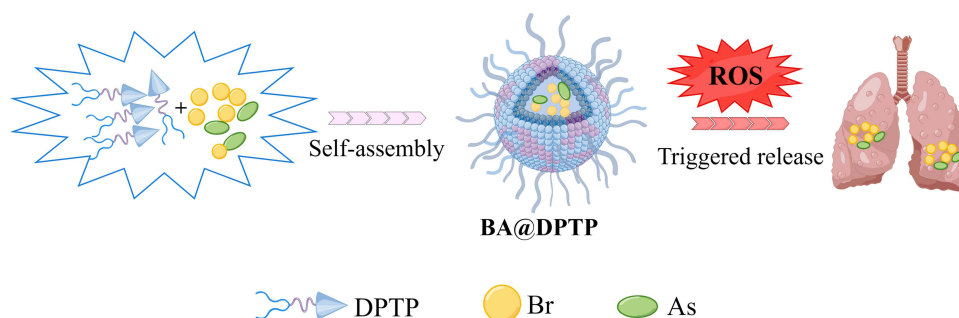


**Figure 2** The schematic diagram of fabrication of BA@DPTP.

red was dissolved in dichloromethane, which was mixed with the dual-drug solution and the aqueous solution of DPTP to prepare the fluorescence-labeled dual-drug nanoplateform following the same procedure. All NPs were filtered through a syringe fiber filter and operated in a biosafety safety cabinet to ensure that they were sterilized for animal studies and cell researches. The morphological images of NPs were taken by using a transmission electron microscope. The hydrodynamic diameter of the NPs was determined by dynamic light scattering and the zeta potential of NPs was measured by laser Doppler electrophoresis on a Zetasizer instrument.

The drug's loading efficiency was acquired by measuring the Br and As content of BA@DPTP by high-performance liquid chromatography (HPLC). Firstly, BA@DPTP suspension was freeze-dried for 12 h, then BA@DPTP (1mg) was dissolved in dichloromethane (0.5 mL) via ultrasonic treatment to completely dissolve BA@DPTP. Secondly, acetonitrile (0.5 mL, HPLC grade) was instilled gradually, and the mixture was put into a fume hood for 12 h to dissolve the drugs, precipitate the polymer and vaporize dichloromethane. Thirdly, the mixture was centrifuged at 1800g for 6 min to remove the precipitations. Fourthly, the supernatant containing the drugs was collected and injected into the HPLC system (20  $\mu$ L). The chromatographic conditions of Br were set as follows: column (C18, 250  $\times$  4.6 mm, 5  $\mu$ m), mobile phase (methanol/acetonitrile/1% glacial acetic acid (86: 10: 4)), flow rate (1.0 mL/min), column temperature (25°C), and detection wavelength (450 nm). The chromatographic conditions of As were set as follows: column (C18, 250  $\times$  4.6 mm, 5  $\mu$ m), mobile phase (acetonitrile/ammonium acetate buffer (40: 60)), flow rate (1.0 mL/min), column temperature (30°C), and detection wavelength (245 nm). Fifthly, the drug concentration in each sample was calculated separately by using the calibration curve established with the known concentrations of Br and As. Finally, the drug loading content (LC) was calculated by the weight ratio of the drug-loaded drug to the drug-loaded NPs and the drug encapsulation efficiency (EE) was calculated by the weight ratios of the loaded drug to the feeding drug.

## ROS-Responsive Drug Release of NPs

Nile red, a hydrophobic fluorescence dye, was encapsulated into the NPs as a model drug to simulate the drug release of NPs as in previous studies.<sup>18</sup>  $\cdot$ OH is a very active and destructive ROS, thus the thioketal bond in the NPs would be easily triggered by  $\cdot$ OH. The Nile red-loaded NPs suspension liquid (0.1 mg/mL) was incubated with 0.25 mM  $\cdot$ OH, 0.5 mM  $\cdot$ OH, and 1 mM  $\cdot$ OH, at 37 °C, respectively. Each sample was repeated 3 times. 150  $\mu$ L NPs suspension liquid was collected and added to a 96 black polystyrene plate. The emission fluorescence (FL) intensity at 607 nm was measured by a microplate reader at an excitation wavelength of 550 nm. The accumulative release of Nile Red was calculated using the following formula:

$$\text{Accumulative release of Nile Red (\%)} = [FL \text{ intensity } (t_0) - FL \text{ intensity } (t_x)] / FL \text{ intensity } (t_0) \times 100\%$$

Where  $t_0$  represents the time at the start and  $t_x$  represents each predetermined time interval.

## Cell Culture in vitro

Mouse pulmonary microvascular endothelial cells (MPMVECs) were obtained as described below. The MPMVECs were cultured in complete DMEM containing 1% (v/v) antibiotic–antimycotic and 15% FBS, 1% ECGS, and 1% P/S.



Different groups were treated as follows: 1#) Sham group: The MPMVECs were stimulated with PBS (10 µg/mL); 2#) LPS group: The MPMVECs were stimulated with LPS (10 µg/mL); 3#) DPTP group: The MPMVECs were stimulated with LPS (10 µg/mL) and DPTP (50 µg/mL); 4#) BR@DPTP group: The MPMVECs were stimulated with LPS (10 µg/mL) and BR@DPTP (50 µg/mL); 5#) AS@DPTP group: The MPMVECs were stimulated with LPS (10 µg/mL) and AS@DPTP (50 µg/mL); 6#) BA@DPTP group: The MPMVECs were stimulated with LPS (10 µg/mL) and BA@DPTP (50 µg/mL). The complete DMEM was stored at 4°C for up to 1 month. The MPMVECs were incubated in an incubator at 37°C, 5% CO<sub>2</sub>, and 100% humidity.

## Isolation and Culture of MPMVECs

To evaluate the therapeutic effect of a dual-drug nano platform on ARDS in vitro, MPMVECs were isolated and cultured from mice according to the previous method of our project team.<sup>27</sup> The fresh lung tissues were isolated from male SPF C57BL/6 mice and immediately immersed in the ice-cold DMEM under sterile conditions. After removing the visceral pleura of the lung tissues, the thin strips of the surrounding lung lobe were obtained and carefully cut into 1–2 mm<sup>2</sup> small pieces. Then, the minced lung tissues were dispersed into a cellular culture flask and incubated with the complete DMEM in the incubator. After incubation for 60 h, the minced lung tissues were removed, and the MPMVECs continued to incubate in the incubator until cells reached 80–90% confluence. Subsequently, MPMVECs were passaged and the complete medium was replaced every 2 days for subsequent experiments.

## Cytotoxicity of NPs

The MPMVECs were seeded in a 96-well culture plate at a density of  $2 \times 10^4$  per well (100 µL) and incubated in the incubator. After 24 h, the complete DMEM was replaced with a medium containing different concentrations of NPs (10 µL). After 12 h of incubation, each well was added CCK-8 solution (10 µL, APE×BIO, USA) while avoiding bubbles for 2 h according to the manufacturer's protocol, followed by measurement of absorbance at 450 nm using a microplate reader (BioTek, USA). The level of LDH in the cell culture medium was measured by the LDH cytotoxicity assay kit.

## Cellular Uptake

To analyze the cellular uptake ability of NPs, the MPMVECs were attached to the special glass dishes. The MPMVECs were firstly stimulated by LPS (10 µg/mL), and then different concentrations of CY5.5-loaded BA@DPTP (0, 125, 250, and 500 µg/mL) were added into the cell medium and incubated for 2 h. Finally, the fluorescence images were taken on a fully automatic live-cell imager (Zeiss, Germany).

## Intracellular ROS Level Inhibition of NPs

The intracellular ROS levels were detected by a ROS detection kit (Beyotime, China). The MPMVECs were attached to a 12-well plate ( $2 \times 10^5$  cells per well) and then stimulated with LPS (10 µg/mL). Next, DPTP (50 µg/mL), BR@DPTP (50 µg/mL), AS@DPTP (50 µg/mL), and BA@DPTP (50 µg/mL) were added into the cell medium and incubated for 12 h. Finally, the MPMVECs were incubated with 2,2'-dichlorodihydrofluorescein diacetate (DCFH-DA) (10 µM) for 30 min at room temperature and taken using an inverted fluorescence microscope (Zeiss, Germany).

## PI Staining

The MPMVECs were attached to the special glass dishes and then stimulated with LPS (10 µg/mL). Next, DPTP (50 µg/mL), BA@DPTP (50 µg/mL), AS@DPTP (50 µg/mL), and BA@DPTP (50 µg/mL) were added into the cell medium and incubated for 12 h. The medium was abandoned, washed with ice-cold PBS one time, and binding buffer two times. All glass dishes were added to the PI solution and observed on a laser-scanning confocal microscope.

## Endothelial Monolayer Permeability Assays

MPMVECs were seeded in the upper chamber of Transwell inserts (Corning, USA) and grown to confluence. The electrical resistance across the MPMVECs' monolayer was monitored by an EVOM2 (World Precision Instruments,

USA) every 2 h. Baseline trans-endothelial electrical resistance (TEER) was measured for 1 h in the pre-experiments. After the challenge of LPS and corresponding treatment, TEER was continuously monitored every 2 h until 12 h.

Similarly, MPMVECs were inoculated to Transwell plates and treated. FITC-dextran (70 kDa, 1 mg/mL) was added to the upper chamber and incubated with the MPMVECs' monolayer for 30 min. The medium was immediately removed from the lower chamber of Transwell plates to a 96-well plate. Finally, the fluorescence intensity of the medium was detected by a microplate reader (excitation wavelength: 493 nm, emission wavelength: 517 nm).

## Cellular Immunofluorescence

The MPMVECs were attached to the special glass dishes with the same treatments as mentioned above. After 12 h of LPS stimulation, the MPMVECs were fixed with paraformaldehyde (4%) for 15 min, ruptured using Triton X-100 solution (0.1%) for 15 min, blocked with BSA (1%) for 1 h at room temperature. Then, the cells were incubated with primary antibodies (p-P65, NLRP3) for 12 h at 4°C and incubated with fluorescent secondary antibody at room temperature for 1 h. Afterward, the cells were incubated with DAPI for 3 min for labeling the nucleus. Finally, the fluorescence images were captured on a laser-scanning confocal microscope (Zeiss LSM880, Germany).

## Animal Experiments

All animal studies were carried out in accordance with the Guide for the Care and Use of Laboratory Animals (NIH Publications No. 8023, revised 1978) and approved by the Animal Ethics Committee of Anhui Medical University (LLSC20221072). SPF, male C57BL/6 mice (6–8 weeks old, 25±2g) were obtained from the Animal Center Anhui Medical University (Anhui, China).

## Animal Model Establishment and Treatment

A well-established mouse ALI model which was performed by intratracheal instillation of LPS (5 mg/kg) was taken as previously described.<sup>28</sup> The mice in the sham group were injected with an equal amount of sterile saline. A half hour after LPS administration, the mice were given different treatments. Different groups were treated as follows: 1#) Sham group: the healthy mice were injected with an equal amount of sterile saline; 2#) LPS group: the ALI mice were intravenously injected with PBS; 3#) DPTP group: the ALI mice were intravenously injected with DPTP (50 mg/kg); 4#) BR@DPTP group: the ALI mice were intravenously injected with BR@DPTP (50 mg/kg); 5#) AS@DPTP group: the ALI mice were intravenously injected with AS@DPTP (50 mg/kg); 6#) BA@DPTP group: the ALI mice were intravenously injected with BA@DPTP (50 mg/kg). The sample injection was performed every 12 h for 24 h. Afterward, the mice were sacrificed to collect the blood samples, bronchoalveolar lavage fluid (BALF), lung tissues, and other organs. In addition, three mice in each group were intravenously injected with 1% EB (dissolved in PBS, 2mL/kg) after 24 h of LPS stimulation. At 1 h after EB administration, the mice were perfused with normal saline through the heart under deep anesthesia to wash the intravascular EB. Subsequently, the lung tissues (100 mg) were removed from each mouse, homogenized in formamide (2 mL), and extracted in a thermostat away from light at 60°C for 24 h. Then, the lung tissue homogenate was centrifuged at 15000g for 20 min to collect the supernatant, and the absorbance of the supernatant was measured at 620 nm. Finally, the EB concentration in each sample was calculated separately by using the calibration curve established with the known concentrations of EB to evaluate the permeability of lung tissue. For the mortality of ALI mice, the mice given the same amount of formulations as described above were challenged with 50 mg/kg LPS (20 mice in each group). The number of daily deaths in each group was monitored until 7 days.

## The Biological Safety Evaluation of NPs in vivo

The brains, hearts, stomachs, livers, spleens, and kidneys of mice were fixed in 4% paraformaldehyde for 24 h and then embedded in paraffin. Paraffin-embedded tissues were cut into serial 4 µm thickness and then stained with hematoxylin and eosin (H&E). Images of the H&E stained sections were collected with the Panoramic tissue quantitative analysis system for histological evaluation. In addition, important indicators of liver and kidney function (ALT, AST, BUN and Scr) were detected for biosafety analysis in vivo.

## NPs Biodistribution in vivo

The mice were injected intravenously with 200  $\mu$ L CY5.5-labeled NPs (50  $\mu$ g/mL) 0.5 h after the ALI model was established. At 2 h after NPs administration, the mice were sacrificed under deep anesthesia, perfused with 1% BSA (dissolved in PBS) through the heart, and imaged by an Illumination Bright Light System LT-9900. Afterward, the brains, hearts, stomachs, spleens, kidneys, livers, and lung tissues were excised for ex-fluorescence imaging. The excitation and emission wavelengths of CY5.5 are 675 nm and 694 nm, respectively.

## Wet/Dry Ratios and EB Content of Lung

The right upper lobes of the lungs were removed from each group of mice ( $n=3$ ) and weighed to obtain the wet weight. Then, the lungs were placed in an oven at 80°C for 48 h to obtain the dry weight. The ratio of wet to dry (W/D) was calculated to evaluate lung edema. Three mice from each experimental group were injected intravenously with Evans blue 1 h before being euthanized to evaluate the permeability of lung tissue by detecting EB content in the lung tissues.

## Lung Histology and Immunohistochemistry

The lung tissues from each group of mice ( $n = 3$ ) were fixed in 4% paraformaldehyde for 24 h and then embedded in paraffin. Paraffin-embedded tissues were cut into serial 4  $\mu$ m thickness and then stained with hematoxylin and eosin (H&E). Images of the H&E stained sections were collected with the Panoramic tissue quantitative analysis system for histological evaluation. Lung injury was assessed by a histologic ALI scoring system as follows: neutrophil infiltration (0–4), hyaline membrane formation (0–4), edema (0–4), and hemorrhage (0–4).<sup>29</sup> The score of each mouse was calculated as the average of 4 lung sections. The remaining lung tissue sections were immunohistochemically stained with primary antibodies against p-P65 and NLRP3 (1:200). Images were captured using the Panoramic tissue quantitative analysis system as mentioned above.

## Collection and Analysis of BALF

The BALF of mice was collected by the lavage of lungs using a tracheal cannula with 0.8 mL of precooled sterile PBS 3 times. Then, the BALF was centrifugated at 4°C, 12,000 g for 30 min to collect the supernatant. The total protein concentrations were determined via a BCA protein assay kit.

## Western Blotting

The total protein was extracted from lung tissues or cells using ice-cold RIPA buffer containing phenylmethylsulfonyl fluoride (1 mM) and phosphotransferase inhibitor (1 mM) on ice for 30min. The lysis solution was centrifugated at 4°C, 12,000 g for 20 min to collect the supernatant, and the protein concentration was quantified with the BCA protein assay Kit. Then equal protein concentration for each sample was processed. After boiling at 100°C 10 min with added 5 $\times$  loading buffer, equivalent amounts of protein samples were loaded onto SDS-PAGE polyacrylamide gels (10%) and then transferred to polyvinylidene difluoride (PVDF) membranes (0.44  $\mu$ m).

Subsequently, the PVDF membranes were blocked in 5% nonfat milk for 1 h at room temperature and then incubated with different primary antibodies at 4°C overnight. Thereafter, the PVDF membranes were washed three times with TBST and incubated with HRP-conjugated secondary antibodies (1:5000) for 1 h at room temperature. Finally, the protein bands were tested using the enhanced chemiluminescent reagent and visualized using the chemiluminescence system.

## Statistical Analysis

The GraphPad Prism 8.0 was used for statistical analysis. All the data were expressed as mean  $\pm$  standard deviation (SD), and a value of  $P < 0.05$  was considered statistically significant. The comparison between the two groups was evaluated by Student's *t*-test, while the differences among multiple experimental groups were evaluated by one-way ANOVA followed by the least significant difference post hoc analysis.

## Results

### Preparation and Characterization of NPs

Owing to the hydrophobic property of Br and As, they were lightly loaded into the amphiphilic DPTP to obtain BA@DPTP, as schematically illustrated in Figure 2. Transmission electron microscopy images showed that both BA@DPTP and DPTP have a spherical shape (Figure 3A). The average hydrodynamic diameter of DPTP was 114 nm (Figure 3B), while that of BA@DPTP increased to 126 nm following Br and As loading (Figure 3C). It should be noted that the diameter of the NPs is larger than that indicated by the TEM images, which is reasonable according to a previous theory.<sup>30</sup>

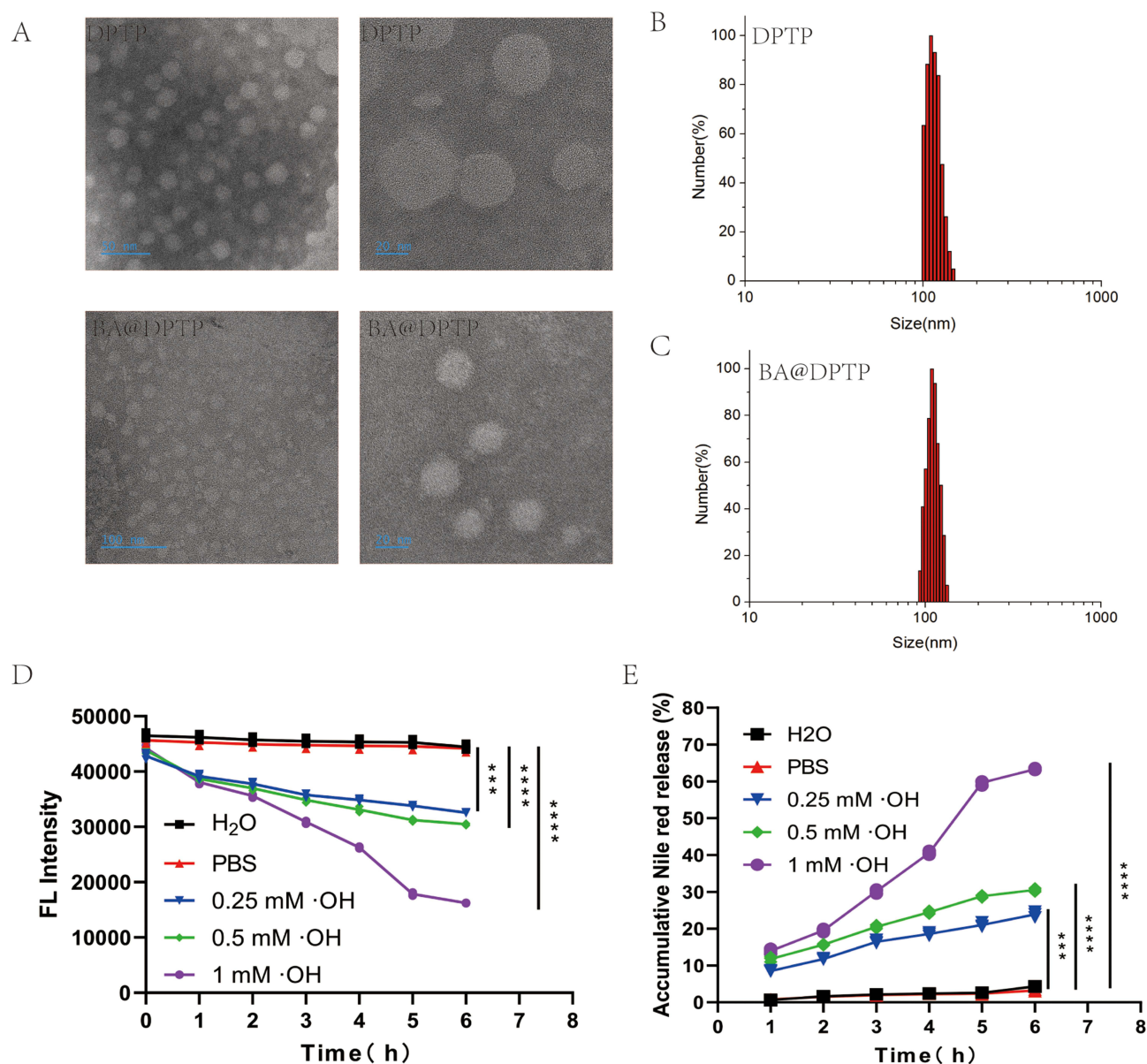


**Figure 3** Characterization of BA@DPTP. (A) Representative transmission electron microscopy(TEM) images of DPTP and BA@DPTP. Size distribution of (B) DPTP and (C) BA@DPTP measured by dynamic light scattering(DLS). (D) FL intensity of Nile red-loaded NPs and (E) accumulative Nile red release after being incubated with H<sub>2</sub>O, PBS, 0.25 mM ·OH, 0.5 mM ·OH, 1 mM ·OH, respectively. \*\*\*p < 0.001, and \*\*\*\*p < 0.0001.



## In vitro Dual-Drug Release Property of the NPs

The fluorescence intensity of Nile red-loaded NPs and accumulative Nile red release were dynamically monitored and calculated after being incubated with H<sub>2</sub>O, PBS, 0.25 mM ·OH, 0.5 mM ·OH, and 1 mM ·OH, at 37°C (Figure 3D and E).

## Cytotoxicity and Cellular Uptake of NPs

MPMVECs were isolated from fresh lung tissues of SPF male C57BL/6 mice using a tissue block attachment method and identified according to our previous methods (Figure S1).<sup>31,32</sup> Cytotoxicity of DPTP and BA@DPTP against MPMVECs were assessed using CCK-8 assay at different concentrations (0, 7.5, 15.5, 31.5, 62.5, 125, 250, and 500 µg/mL) of the NPs. As shown in Figure 4A and B, the DPTP and BA@DPTP displayed no obvious cytotoxicity at concentrations ranging from 7.5 to 500 µg/mL following 12 h and 24 h of exposure. The levels of LDH in the culture medium of each group were examined to determine the integrity of MPMVECs.<sup>33</sup> The LDH level in the culture medium was increased

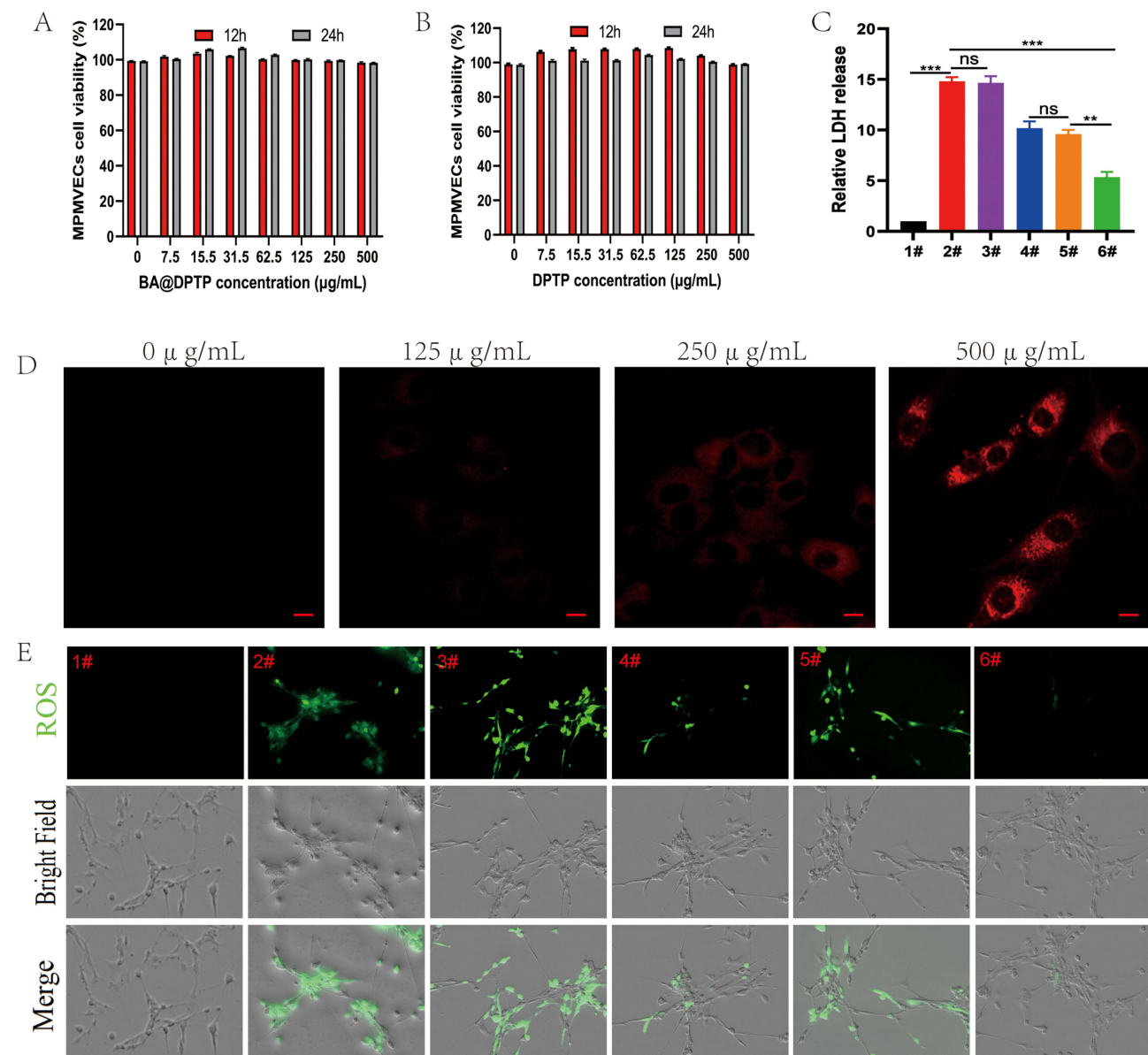


**Figure 4** Cell viability assay of MPMVECs incubated with (A) DPTP and (B) BA@DPTP at different concentrations (0, 7.5, 15.5, 31.5, 62.5, 125, 250 and 500 µg/mL) every 12 h. (C) Relative LDH level in the cell culture medium (n=3, t-test). (D) Fluorescence live cell imaging at different concentrations of BA@DPTP (0, 125, 250 and 500 µg/mL). The NPs were labeled with fluorescence (red). Scale bar, 10 µm. (E) ROS measurement of MPMVECs after different samples treatment and LPS (10 µg/mL) stimulation for 12 h (200 ×). \*\*p < 0.01, \*\*\*p < 0.001, and ns indicates no significant.



significantly by LPS, whereas treatment with the NPs reversed this change (Figure 4C). The administration of BR@DPTP and AS@DPTP could reduce LDH levels, while BA@DPTP had the most significant ability to reduce LDH. We next assessed the cellular uptake of BA@DPTP in vitro by MPMVECs using fluorescence microscopy. To examine NPs uptake under inflammatory conditions, the MPMVECs were stimulated by LPS (10 µg/mL). As shown in Figure 4D, BA@DPTP could be easily internalized when incubated with LPS for 2 h, and their uptake amount increased with increasing concentration of BA@DPTP. At the concentration of 500 µg/mL, the MPMVECs showed the strongest endocytosis of BA@DPTP. The internalized NPs were predominantly located in the cytoplasm. None of the NPs could penetrate the nuclei, which was expected because they are much larger in size than nuclear pores (25–30 nm).<sup>34</sup>

## Effects of BA@DPTP on LPS-Treated MPMVECs in vitro

DCFH-DA was used to specifically detect the ROS levels in different experimental groups as shown in Figure 4E. ROS were excessively expressed after LPS (10 µg/mL) stimulation, with increased bright green fluorescence noted in the MPMVECs. The DPTP and AS@DPTP treatment groups did not show reduced ROS levels compared with the LPS group in the MPMVECs. The BR@DPTP-treated group showed significantly increased inhibition of ROS production compared with that in the LPS, LPS + DPTP, and LPS + AS@DPTP groups.

Next, a PI fluorescence staining assay was utilized to comprehensively detect the anti-pyroptosis effect in different groups (Figure 5A). Pyroptotic cells showed obvious swelling with pathognomonic large bubbles on the plasma membrane under a bright field, as described in a previous study.<sup>35</sup> The pyroptotic cells showed red fluorescence under the fluorescence field since PI passes through the plasma membrane of pyroptotic cells to reach the cell interior (Figure S2). As shown in Figure 5B, LPS administration significantly increased the ratio of apoptotic cells. When treated only with DPTP, there was no change in the rate of apoptosis. In comparison to DPTP, the BR@DPTP treatment reduced the percentage of apoptotic cells. In the AS@DPTP-treated group, there was a more significant inhibition in the rate of apoptosis compared with the LPS, LPS + DPTP, and LPS + BR@DPTP groups.

The scheme to show the principle of TEER in Figure 5C. In order to investigate the effect of the dual-drug nanoplatform on MPMVEC barrier function, we measured endothelial monolayer permeability by continuously monitoring the changes in the TEER values every 2 h until 12 h and FITC-dextran leakage at 12 h, as schematically illustrated in Figure 5D. LPS administration destroyed MPMVEC barrier function and enhanced endothelial monolayer permeability, showing a gradual decrease in TEER values in a time-dependent manner (Figure 5E). The TEER value and FITC-dextran leakage did not change after DPTP treatment alone, and they were improved after BR@DPTP and AS@DPTP treatments. Notably, BA@DPTP treatment significantly improved the TEER value and ameliorated FITC-dextran leakage (Figure 5F).

## Mechanism of Inflammatory Suppression in MPMVECs

We performed Western blotting (WB), enzyme-linked immunosorbent assay (ELISA), and immunofluorescence (IF) assays in MPMVECs to further analyze the mechanism of the dual-drug nanoplatform against ARDS. The protein levels analysis indicated that BR@DPTP decreased phosphorylation of NF-κB (Figure 6A and B) and AS@DPTP reduced the expression of pyroptosis-related proteins (Figure 6C–F), while BA@DPTP simultaneously downregulated phosphorylation of NF-κB and the expression of pyroptosis-related proteins. Besides, ELISA analysis showed that IL-1β (Figure 6G), IL-18 (Figure 6H), and TNF-α (Figure 6I) levels in cellular supernatant were significantly increased after LPS (10 µg/mL) stimulation compared with that in the sham group. The treatment with independent empty nanocarrier DPTP did not affect the proinflammatory cytokines. Following treatment with BR@DPTP, AS@DPTP, and BA@DPTP, levels of the proinflammatory cytokines were reduced to various degrees, with the most significant reduction observed in the BA@DPTP group. Furthermore, IF images of MPMVECs (Figure 6J–L) revealed that the fluorescence intensity of NLRP3 increased significantly in the cytoplasm while that of p-P65 increased obviously in the nucleus after the LPS challenge for 12 h, which were consistent with the WB results. The fluorescence intensity of NLRP3 and p-P65 weakened accordingly after treated with BR@DPTP, AS@DPTP, and BA@DPTP.

## Small animal imaging and biological safety evaluation of BA@DPTP in vivo

Small animal imaging was implemented in an established LPS-induced ALI mouse model to assess whether BA@DPTP has good penetrative ability and targeting property in inflamed mouse lung tissues. The CY5.5-labeled BA@DPTP was injected

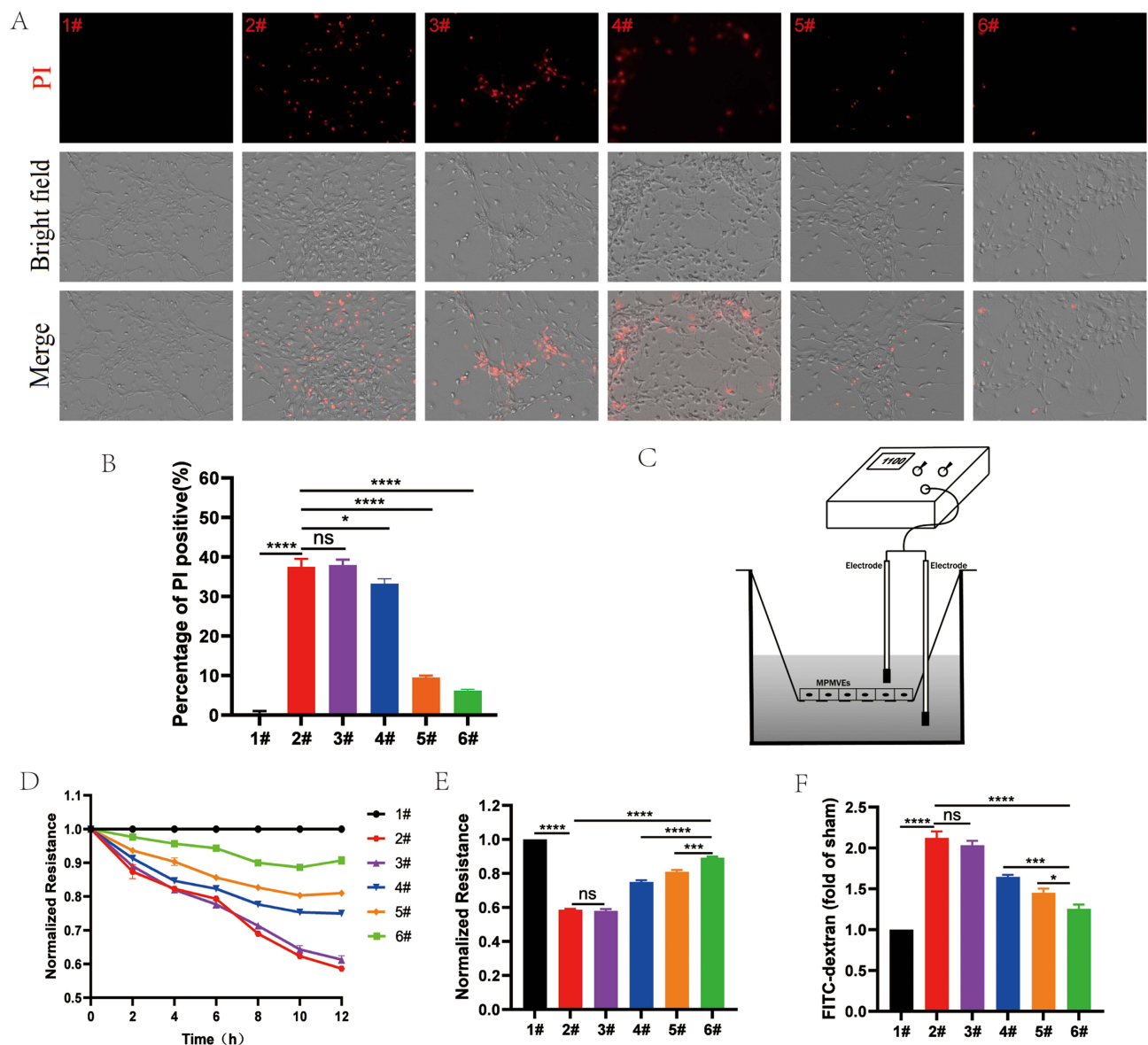


**Figure 5** (A) PI fluorescence staining of MPMVECs after different samples treatment and LPS (10  $\mu\text{g/mL}$ ) stimulation for 12 h (100  $\times$ ). (B) Percentage of MPMVECs with PI fluorescence staining positive ( $n=3$ ,  $t$ -test). (C) The scheme to show the principle of TEER. (D) The TEER values were continuously monitored every 2 h during LPS treatment ( $n=3$ ), which are the ratio of the monitoring value of each treatment group to the monitoring value of the sham. The (E) TEER values and (F) FITC-dextran flux were determined after LPS stimulation for 12 h ( $n=3$ ,  $t$ -test). \* $p < 0.05$ , \*\*\* $p < 0.001$ , and \*\*\*\* $p < 0.0001$ ; ns indicates no significant.

into the ALI mice via the tail vein after 1 h of pretreatment with intratracheally administered LPS (10 mg/kg). Subsequently, the ROS in the inflammatory microenvironment of ALI could trigger the TK bond of the nanocarrier to degrade the nanoplatform and thereby release the drugs. In vivo fluorescence imaging of necropsied mice (Figure 7A) and ex vivo fluorescence imaging of resected tissues (Figure 7B) showed a strong and concentrated fluorescence intensity in the lung tissue at 1 h after intravenous administration, indicating that BA@DPTP had a favorable targeting effect in the mouse model of ALI. Furthermore, we also examined whether BA@DPTP exerted harmful effects on other vital organs such as the brain, heart, stomach, liver, spleen, and kidney. H&E staining showed no indications of tissue damage or focal architecture distortion and the important indicators of liver and kidney function in all groups were in the normal range, indicating that BA@DPTP did not have any observable toxicity (Figure S3 and Table S).

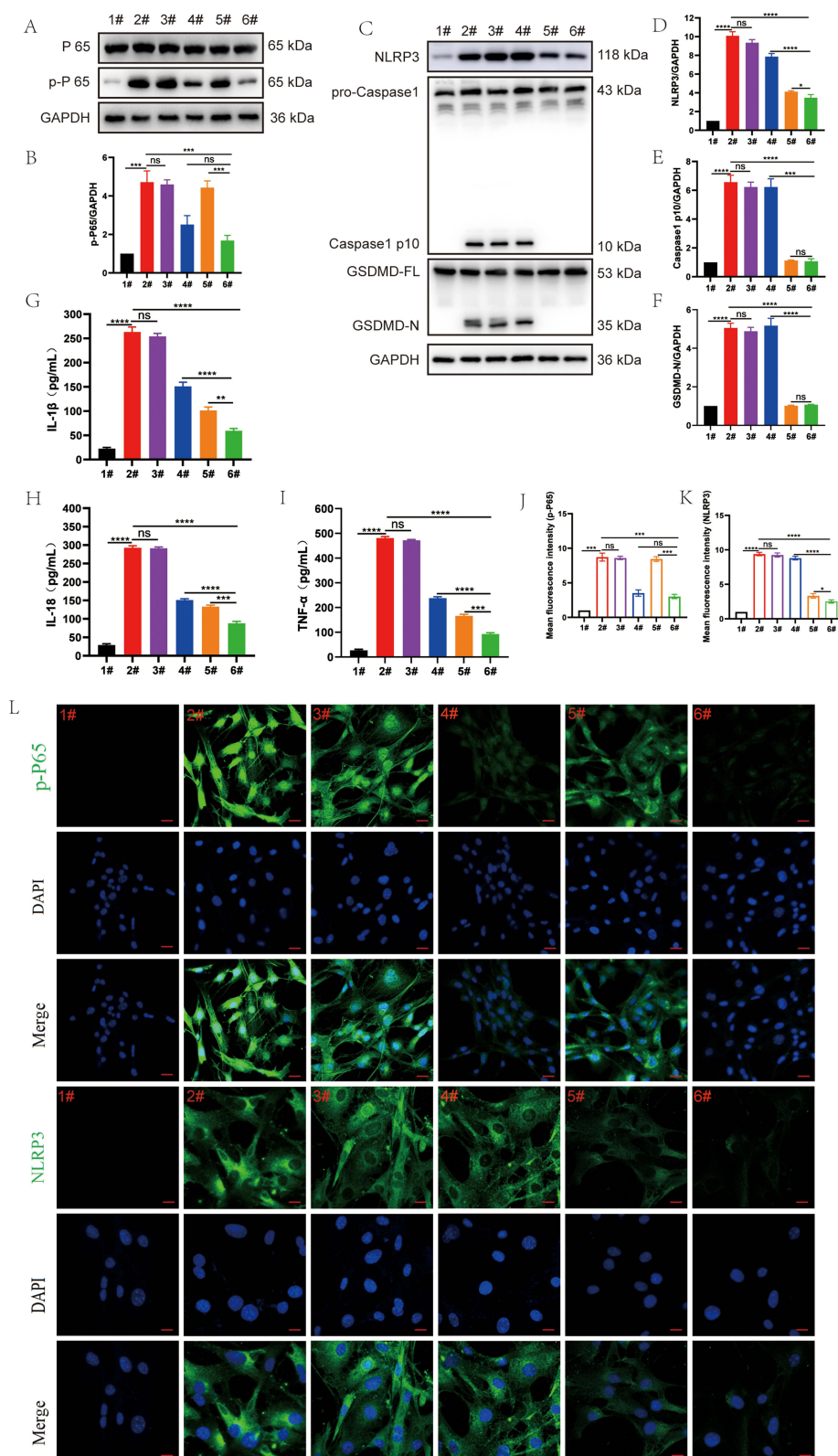


**Figure 6** The mechanism of BA@DPTP suppressing inflammation in MPMVECs. (A) Western blotting analysis of NF- $\kappa$ B signal pathway and quantitative analysis of (B) p-P65 (n=3, t-test) in MPMVECs. (C) Western blotting analysis of NLRP3/caspase-1/GSDMD-dependent pyroptosis and quantitative analysis of (D) NLRP3, (E) Caspase1 p10 and (F) GSDMD-N (n=3, t-test) in MPMVECs. (G) IL-1 $\beta$ , (H) IL-18, and (I) TNF- $\alpha$  levels in cellular supernatant were measured by ELISA (n=3, t-test). The mean fluorescence intensity of (J) p-P65 and (K) NLRP3 were analyzed (n=3, t-test). (L) Immunofluorescence staining of p-P65 and NLRP3 in MPMVECs. Nuclei were stained with DAPI. (scale bar: 20  $\mu$ m). \*p < 0.05, \*\*p < 0.01, \*\*\*p < 0.001, and \*\*\*\*p < 0.0001; ns indicates no significant.



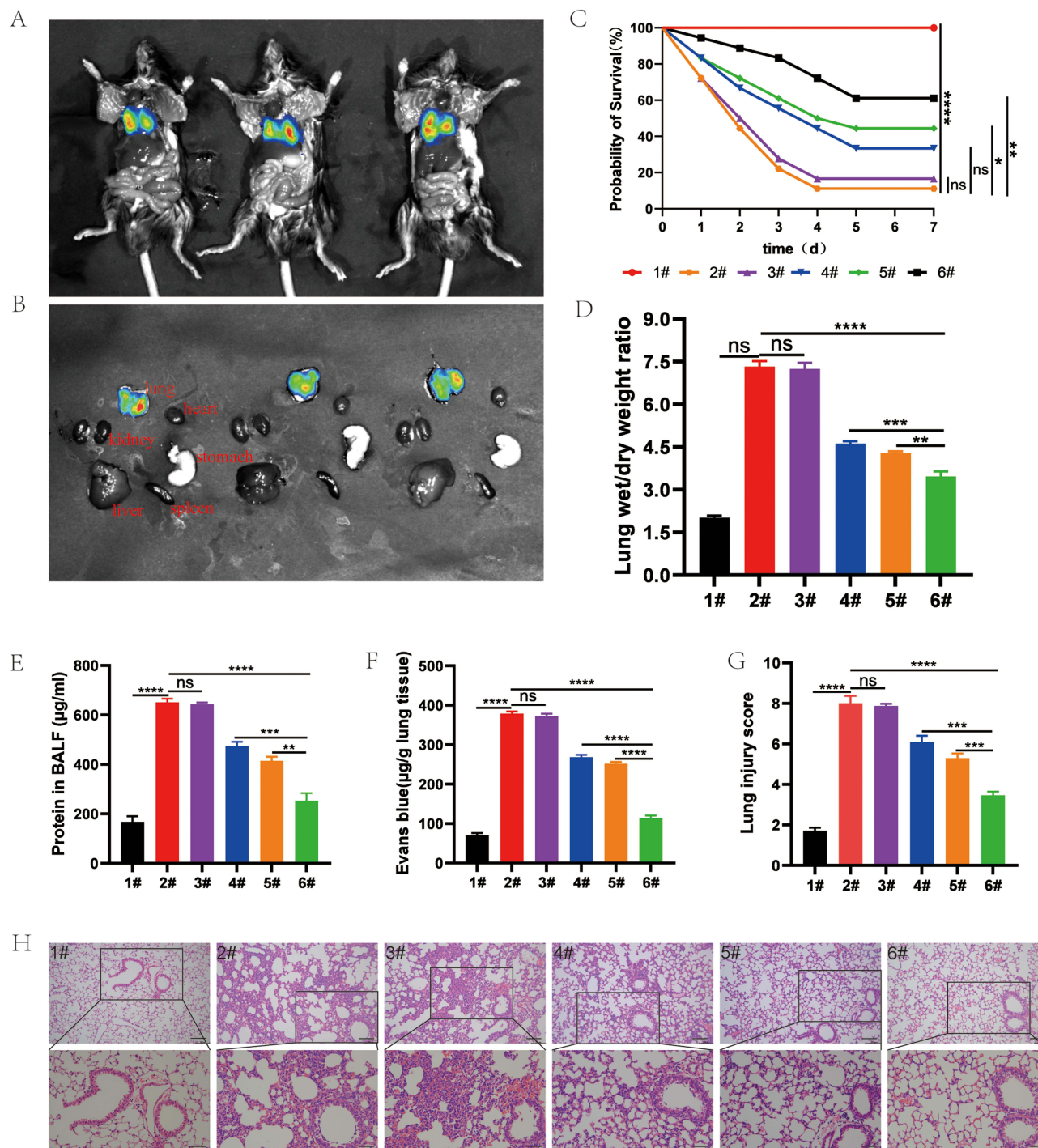


**Figure 7** BA@DPTP ameliorate LPS-induced ALI in mice. **(A)** In vivo fluorescence imaging of necropsied mice and **(B)** ex vivo fluorescence imaging of resected tissues. **(C)** Mice survival curve.  $n = 20$  mice/group (Log Rank test). **(D)** The lung wet/dry weight ratio, **(E)** BALF total protein concentration and **(F)** EB Extravasation ( $n=3$ ,  $t$ -test). **(G)** Lung injury score ( $n=3$ ,  $t$ -test). **(H)** Lung histopathological features. Scale = 100  $\mu\text{m}$  and Scale = 50  $\mu\text{m}$ . \* $p < 0.05$ , \*\* $p < 0.01$ , \*\*\* $p < 0.001$ , and \*\*\*\* $p < 0.0001$ ; ns indicates no significant.

## Therapeutic Activity of NPs in ALI Mice

We further tested the therapeutic efficacy of BA@DPTP on LPS-induced ALI in mice. A survival curve was drawn by monitoring the number of mouse deaths per 24 h until 7 d after 50 mg/kg LPS administration (Figure 7C). The survival curve suggested that the mortality rate of mice in the LPS group on the first day was 25% and that on the 7th day was as

high as 90%. The mortality rate in the LPS + DPTP group without drug loading was similar to that observed for the LPS group. The mortality rates in the LPS + BR@DPTP and LPS + AS@DPTP groups were slightly better, but the LPS + BR@DPTP group had no statistically significant difference ( $P > 0.05$ ) and the LPS + AS@DPTP group had a statistically significant difference ( $P < 0.05$ ) compared with LPS group. Notably, treatment with BA@DPTP could lengthen the survival time and significantly increase the 7-day survival rate to 65%.

As shown in Figure 7D, the mice in the ALI model group had the highest lung W/D ratio, indicating that they had severe pulmonary edema. There was no significant difference in the degree of pulmonary edema between the DPTP-treated group and the model group. The BR@DPTP and AS@DPTP showed suppression of pulmonary edema to a certain extent, while BA@DPTP significantly reduced the lung W/D ratio compared with that in the model group. These findings indicate that BA@DPTP can excellently inhibit pulmonary edema in ALI. The total protein concentrations in BALF (Figure 7E) indicated that the model group had the highest permeability of the capillary endothelial-alveolar epithelial barrier. The BA@DPTP-treated mice had the lowest total protein concentrations in BALF compared with that in all other groups, except the sham group. As shown in Figure 7F, the analyses of EB extravasation in the lung tissue further revealed the lowest permeability of capillary endothelial-alveolar epithelial barrier and degree of lung injury in the LPS + BA@DPTP group compared with that in all other groups, except the sham group. The results of the lung W/D ratio, total protein concentrations in BALF, and EB extravasation in the lung tissue demonstrated the therapeutic efficiency of BA@DPTP.

Consistent with the above findings, the H&E staining of pathological sections of the ALI model group showed the most severe neutrophil infiltration, alveolar septal thickening, and alveolar collapse in the lung tissues, as shown in Figure 7H. The administration of BR@DPTP and AS@DPTP could ameliorate histological tissue injury, whereas BA@DPTP could significantly reduce the histological lung tissue injury, as verified by the smallest ALI score using a histologic ALI scoring system, as shown in Figure 7G.<sup>29</sup> Furthermore, the levels of the inflammatory factors IL-1 $\beta$  (Figure 8A), IL-18 (Figure 8B), and TNF- $\alpha$  (Figure 8C) in the serum were more reduced by BA@DPTP than by BR@DPTP or AS@DPTP.

## In vivo inhibition of NF- $\kappa$ B signal pathway and pyroptosis by BA@DPTP

WB and immunohistochemistry (IHC) assays were performed to further clarify the mechanism underlying the therapeutic effects of BA@DPTP in ALI mice. The protein levels analysis revealed that BR@DPTP decreased LPS-induced phosphorylation of NF- $\kappa$ B (Figure 8D and E), and AS@DPTP reduced the expression of NLRP3 and decreased the activation of the caspase-1-dependent gasdermin D (GSDMD) pore formation (Figure 8F–I), which causes pyroptosis in the lung tissues in ALI.<sup>36</sup> Importantly, BA@DPTP significantly downregulated both phosphorylation of NF- $\kappa$ B and the expression of pyroptosis-related proteins. Immunohistochemical analysis was further performed to evaluate the expression profiles of p-P65 and NLRP3 (Figure 8J). The positive expression levels of p-P65 and NLRP3 were the highest in the LPS group and the lowest in the sham group among the six groups. Following treatment with DPTP, this expression pattern was not significantly altered. However, following treatment with BR@DPTP, AS@DPTP, and BA@DPTP, the expression pattern was inverted at different levels. p-P65, one of the hallmarks of oxidative stress, was downregulated in BR@DPTP and BA@DPTP groups. NLRP3, an important protein that initiates pyroptosis, was downregulated in the AS@DPTP group and BA@DPTP group. These reduced expression levels of p-P65 and NLRP3 in the BA@DPTP treatment group compared with that in other groups is consistent with the WB results in vivo.

## Discussion

During acute inflammation, ROS participates in the elimination of foreign particles and pathogens; however, its overproduction can lead to tissue damage such as in ARDS.<sup>37</sup> Therefore, reducing ROS is a promising strategy to alleviate oxidative stress in ARDS. Br has been shown to have a strong ability to resist oxidative stress,<sup>22,23</sup> and statins have certain efficacy in the treatment of ARDS.<sup>24</sup> In this study, Br and As were used to synergistically treat ARDS, but Br and As are hydrophobic. Intravenous injection is an important drug-delivery route in clinical practice. Further, we aim to design a carrier that will allow hydrophobic Br and As to be used intravenously, while increasing its targeting capability and reducing its potential side effects. Based on these objectives, a ROS-triggered amphiphilic nanocarrier DPTP was successfully created to realize the intelligent release of Br and As.



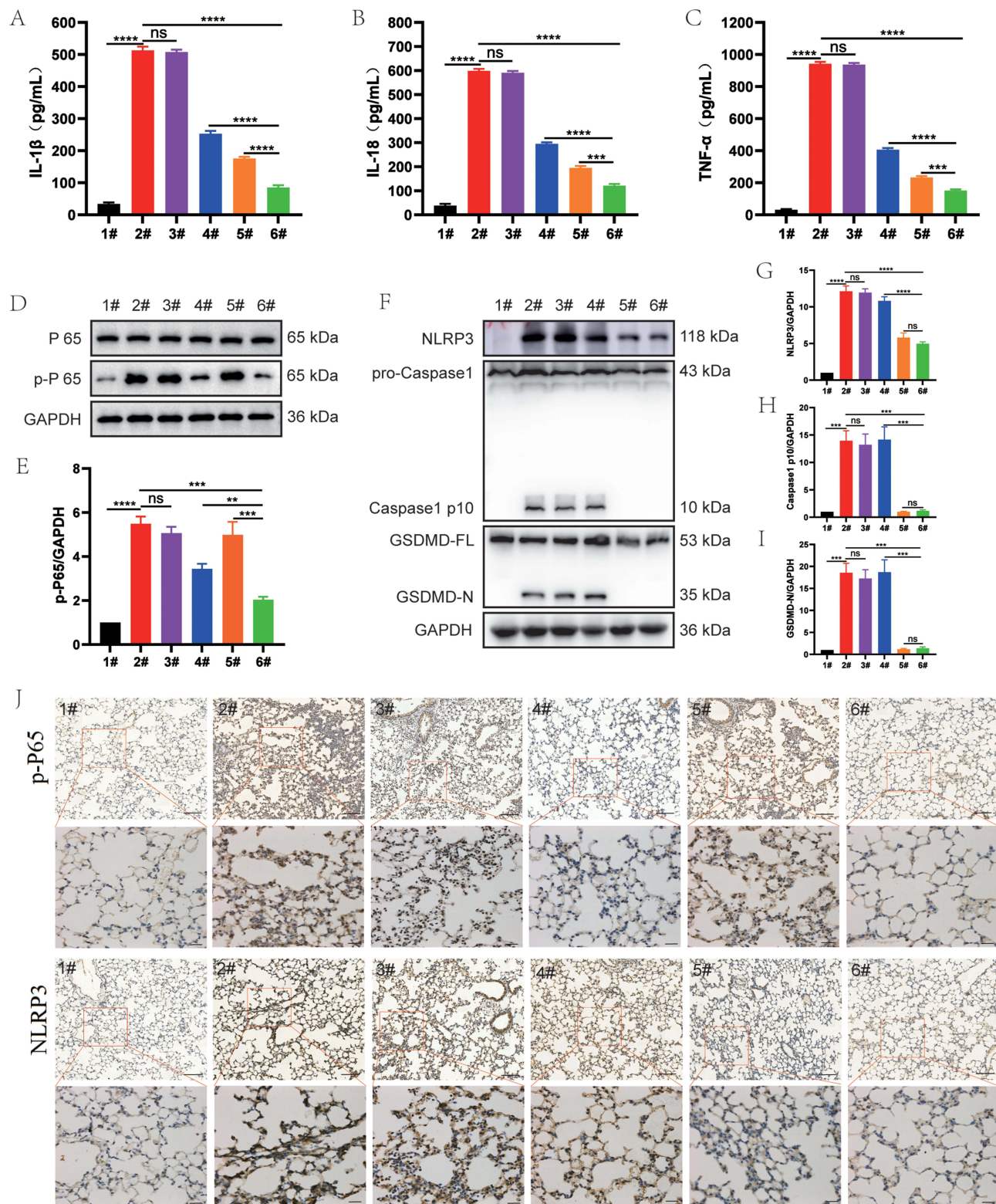


**Figure 8** The mechanism of BA@DPTP suppressing inflammation in LPS-induced ALI mice. (A) IL-1 $\beta$ , (B) IL-18, and (C) TNF- $\alpha$  levels in the serum were measured by ELISA ( $n=3$ ,  $t$ -test). (D) Western blotting analysis of NF- $\kappa$ B signal pathway and (E) quantitative analysis of p-P65 ( $n=3$ ,  $t$ -test). (F) Representative Western blotting analysis of NLRP3/caspase-1/GSDMD-dependent pyroptosis and quantitative analysis of (G) NLRP3, (H) Caspase 1 p10 and (I) GSDMD-N ( $n=3$ ,  $t$ -test) in mice lung from each group. (J) Representative immunohistochemical images of p-P65 and NLRP3 protein in the lungs. Scale = 100  $\mu$ m; Scale = 50  $\mu$ m. \*\* $p < 0.01$ , \*\*\* $p < 0.001$ , and \*\*\*\* $p < 0.0001$ ; ns indicates no significant.

The hydrophobic Br and As were simultaneously encapsulated in the amphiphilic nanocarrier DPTP involving a thioketal bond to obtain the hydrophilic ROS-responsive nanoparticles named BA@DPTP. The BA@DPTP would be triggered by ROS, degraded to release encapsulated Br and As on-demand at pulmonary inflammatory tissues, thereby creating an intelligent adaptive NP system for transporting drugs. Nile red-loaded NPs were used to monitor drug release as Nile red is a hydrophobic fluorescence dye.<sup>38</sup> The  $\cdot\text{OH}$  species is a destructive and active ROS,<sup>18</sup> and hence, may potentially trigger drug release. The fluorescence intensity of the NPs gradually decreased with increasing duration of  $\cdot\text{OH}$  treatment, with higher levels of  $\cdot\text{OH}$  resulting in faster drug release, which fully indicates that BA@DPTP can be triggered by the ROS in lung tissue of ALI. The fluorescence intensity of the NPs did not change over time in H<sub>2</sub>O and PBS, which further suggests that the drugs (Br and As) can be excellently maintained in the NPs during transportation.

Pulmonary microvascular endothelial barrier damage is the prominent pathophysiological characterization of ARDS, and it is closely associated with the exudation of protein-rich edema fluid and the infiltration of inflammatory cells in the alveolar space.<sup>1,7</sup> Therefore, we isolated and cultured the MPMVECs from C57BL/6 mice for the study of ARDS. LPS is an integral component of the cell wall of Gram-negative bacteria, has been widely used in cells and animals for experimental research on ARDS.<sup>39,40</sup> BA@DPTP can be efficiently internalized by inflamed MPMVECs induced by LPS, suggesting that it may be possible to achieve the release of Br and As inside and around damaged MPMVECs and subsequently reverse the cell damage. In living cells, ROS are formed as a natural by-product of the normal metabolism of oxygen by mitochondria and play an important role in cell signaling and homeostasis.<sup>41,42</sup> However, excessive ROS production is related to the destruction of the microscopic structure and function of cells, which is called oxidative stress.<sup>42–44</sup> In ARDS, mitochondria can show excessive ROS accumulation and are often seriously damaged.<sup>45,46</sup> The detection of ROS levels results confirmed that Br-loaded NPs have excellent anti-oxidative stress effects, which is consistent with previous studies.<sup>47,48</sup> However, BA@DPTP had the strongest ROS scavenging effect because of the combined influence of the drugs. According to the PI fluorescence staining results, As-loaded NPs have significant anti-pyroptosis effects is consistent with previous findings that statins can inhibit pyroptosis,<sup>49</sup> and BA@DPTP had the strongest suppression effect on cell pyroptosis. BR@DPTP inhibited the NF- $\kappa$ B signal pathway and AS@DPTP inhibited the NLRP3/caspase-1/GSDMD-dependent pyroptosis in MPMVECs. Furthermore, the combination of Br and As in BA@DPTP can better protect MPMVECs against LPS-induced barrier disruption. The damage of the MPMVECs barrier was effectively suppressed by BA@DPTP during inflammation.

The lung is considered the most important organ for gas exchange, and the pulmonary vascular system occupies 25–30% of the entire endothelial surface in the vascular network.<sup>50</sup> It has been reported that enhanced pulmonary endothelial permeability could last for quite a long time in ARDS animal models.<sup>51</sup> Owing to nanoscale dimensions, nanoplateforms can achieve passive targeting of sites of injury after systemic administration taking advantage of the leaky blood vascular system in the injured tissues.<sup>52,53</sup> Furthermore, NPs rapidly accumulate in injured lungs within a few hours, which is attributed to the elevated permeability caused by the damage of the pulmonary capillary endothelial-alveolar epithelial barrier.<sup>54</sup> In addition, inflamed tissues can release and accumulate a large amount of ROS.<sup>37</sup> The current study synthesized a ROS-triggered nanocarrier DPTP, whereby drugs are only expected to be released in inflamed lung tissues. Small animal imagings and histochemical fluorescence images suggested that BA@DPTP accumulated in the inflammatory lungs of ALI and showed satisfactory targeted drug delivery.

The prominent pathophysiological features of ARDS are reduced lung volume, low pulmonary compliance, and disproportionate ventilation flow ratio, which are caused by pulmonary edema and alveolar collapse due to the influx of protein-rich edema fluid into the air spaces and the infiltration of inflammatory cells as a result of increased permeability of capillary endothelial-alveolar epithelial barrier.<sup>10</sup> In our study, the permeability of the capillary endothelial-alveolar epithelial barrier was assessed based on the total protein concentrations in BALF, the content of Evans Blue in lung tissue, and the lung wet/dry (W/D) ratio. The lung W/D ratio is an appropriate and typical index of pulmonary edema as it is a simple, maneuverable, and intuitionistic characteristic.<sup>29</sup> It is worth mentioning that the dual-drug loaded NP BA@DPTP excellently suppressed the increase in the permeability of the capillary endothelial-alveolar epithelial barrier in ALI mice. While Br and As are often used in clinical practice of other diseases,<sup>21,55</sup> we have confirmed that BA@DPTP was able to effectively suppress the infiltration of inflammatory cells in lung tissue and inflammatory response, inhibit the influx of protein-rich edema fluid into the pulmonary alveolar and interval, improve alveolar collapse, and reduce the mortality of ALI mice. The proteins level analyses demonstrated that BA@DPTP suppresses the lung injury in ALI mainly by inhibiting the NF- $\kappa$ B signal pathway and

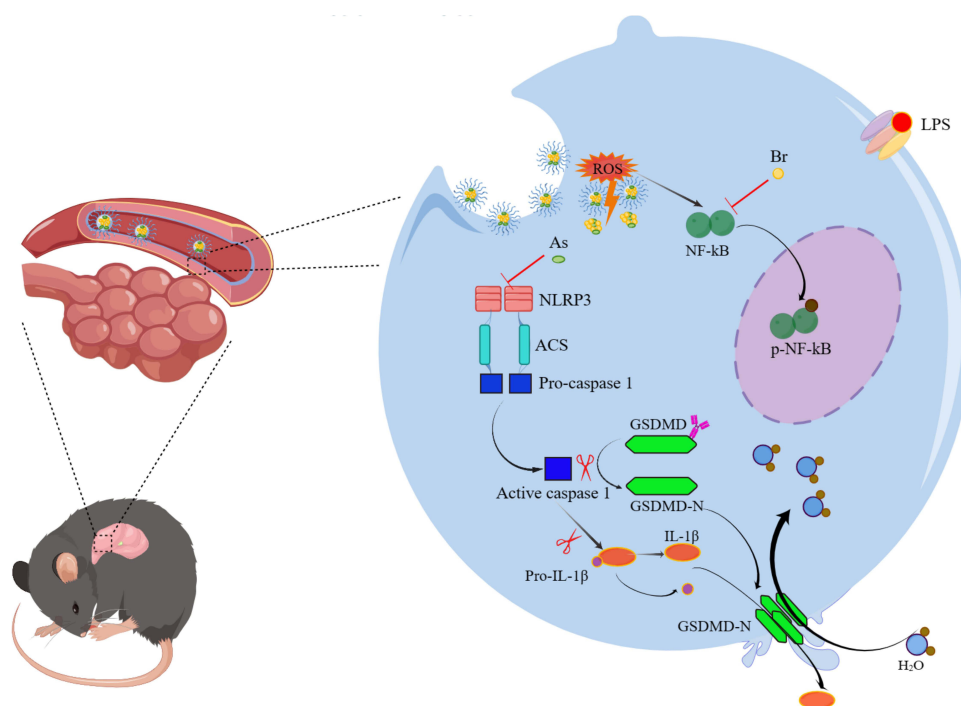


**Figure 9** The mechanism of BA@DPTP with targeting of inflammatory lung tissues for ARDS therapy.

NLRP3/caspase-1/GSDMD-dependent pyroptosis, and there is a synergistic effect between the Br and As. The detailed mechanism of the dual-drug delivery intelligent nanoplatform described with inflammatory pulmonary site-targeting effect for ALI therapy is depicted in Figure 9.

Our study showed that the combination of Br and As has a synergistic effect on reversing abnormal changes and restoring homeostasis of the pulmonary environment. This dual targeting system can not only achieve targeted delivery to inflammation sites, but also enhance drug anti-oxidative activity and inhibit pyroptosis. BA@DPTP has the potential to reduce the infiltration of inflammatory cells in the lung tissues, inhibit the flow of protein-rich edema fluid into the alveoli, and retain the normal physiological structure of the lung tissue. Taken together, BA@DPP could be a promising candidate in the treatment of ALI.

There are several limitations in our study. First, the NPs may be effective not only on MPMVECs in ALI but also on other cells in lung tissue. However, this study did not investigate exactly which cells the NPs have therapeutic effect on. In addition, the NPs could accumulate in the inflammatory lung via a passive targeting strategy and intelligently release drugs in inflamed tissues by ROS-response bond. The NPs did not target-specific organelles of damaged cells. In future studies, we intend to not only improve the modification of the current material, but also investigate its therapeutic effect on other cells.

## Conclusion

Based on the key pathophysiological process of ARDS that is the disruption of the pulmonary endothelial barrier,<sup>9–11</sup> we simultaneously encapsulated Br and As in the ROS-responsive DPTP to obtain BA@DPTP for enhanced precise therapy of ALI. BA@DPTP not only effectively retained the integrity of the pulmonary structure but also reduced the mortality of ALI mice. BA@DPTP could accumulate in inflammatory pulmonary sites through a passive targeting strategy and intelligently release Br and As only in the inflammatory tissue via ROS-responsive bond, thereby enhancing the drugs' effectiveness and markedly reducing side effects. Br was effective to inhibit the activation of P-65 to suppress oxidative stress and As improved pyroptosis by inhibiting the activation of Caspase 1, the synergy of BA@DPTP can be achieved through pleiotropic pharmacological mechanisms. Our study confirmed that single Br or As was not effectively improve ALI, while we verified that the combination of Br and As significantly decreased the disruption of the pulmonary endothelial barrier to achieve the perfect therapeutic effect of ALI. In addition, Br and As are hydrophobic and only can be administered orally in clinical practice. Fortunately, BA@DPTP displayed a favorable feature in drug delivery, especially for improving solubility of Br and As. BA@DPTP can be administered



intravenously which brings great benefits to critically ill patients who cannot be administered orally. Our study provided an promising candidate for enhanced precise therapy of ARDS.

## Acknowledgments

This work was supported by the National Natural Science Foundation of China (No. 81974292). The study would like to thank The Center for Scientific Research of Anhui Medical University for providing technical assistance.

## Disclosure

The authors report no conflicts of interest in this work.

## References

1. Fan E, Brodie D, Slutsky AS. Acute Respiratory Distress Syndrome: advances in Diagnosis and Treatment. *JAMA*. 2018;319(7):698–710. doi:10.1001/jama.2017.21907
2. Rubenfeld GD, Caldwell E, Peabody E, et al. Incidence and outcomes of acute lung injury. *N Engl J Med*. 2005;353(16):1685–1693. doi:10.1056/NEJMoa050333
3. Bellani G, Laffey JG, Pham T, et al. Epidemiology, Patterns of Care, and Mortality for Patients With Acute Respiratory Distress Syndrome in Intensive Care Units in 50 Countries. *JAMA*. 2016;315:788–800. doi:10.1001/jama.2016.0291
4. Peiris JS, Yuen KY, Osterhaus AD, et al. The severe acute respiratory syndrome. *N Engl J Med*. 2003;349(25):2431–2441. doi:10.1056/NEJMra032498
5. Zumla A, Hui DS, Perlman S. Middle East respiratory syndrome. *Lancet*. 2015;386(9997):995–1007. doi:10.1016/S0140-6736(15)60454-8
6. WHO. Coronavirus Disease (COVID-19) Pandemic. Available from: <https://www.who.int/emergencies/diseases/novel-coronavirus-2019>. Accessed February 13, 2024.
7. Matthay MA, Zemans RL, Zimmerman GA, et al. Acute respiratory distress syndrome. *Nat Rev Dis Primers*. 2019;5(1):18. doi:10.1038/s41572-019-0069-0
8. Xabi M, Cristiane SC, Claus ML. Overcoming the pulmonary barrier: new insights to improve the efficiency of inhaled therapeutics. *Eur J Nanomed*. 2014;6:157–169.
9. Matthay MA, Ware LB, Zimmerman GA. The acute respiratory distress syndrome. *J Clin Invest*. 2012;122(8):2731–2740. doi:10.1172/JCI60331
10. Thompson BT, Chambers RC, Liu KD. Acute Respiratory Distress Syndrome. *N Engl J Med*. 2017;377:562–572. doi:10.1056/NEJMra1608077
11. Rezoagli E, Fumagalli R, Bellani G. Definition and epidemiology of acute respiratory distress syndrome. *Ann Transl Med*. 2017;5(14):282. doi:10.21037/atm.2017.06.62
12. Cheng KT, Xiong S, Ye Z, et al. Caspase-11-mediated endothelial pyroptosis underlies endotoxemia-induced lung injury. *J Clin Invest*. 2017;127(11):4124–4135. doi:10.1172/JCI94495
13. Mehta D, Malik AB. Signaling mechanisms regulating endothelial permeability. *Physiol Rev*. 2006;86(1):279–367. doi:10.1152/physrev.00012.2005
14. Nourshargh S, Alon R. Leukocyte migration into inflamed tissues. *Immunity*. 2014;41(5):694–707. doi:10.1016/j.immuni.2014.10.008
15. Qiao Q, Liu X, Yang T, et al. Nanomedicine for acute respiratory distress syndrome: the latest application, targeting strategy, and rational design. *Acta Pharm Sin B*. 2021;11(10):3060–3091. doi:10.1016/j.apsb.2021.04.023
16. Ji H, Zhang C, Xu F, et al. Inhaled Pro-Efferocytic Nanozymes Promote Resolution of Acute Lung Injury. *Adv Sci (Weinh)*. 2022;9(26):e2201696. doi:10.1002/advs.202201696
17. Thompson BT, Chambers RC, Liu KD. Acute Respiratory Distress Syndrome. *N Engl J Med*. 2017;377:1904–1905.
18. Zhai Z, Ouyang W, Yao Y, et al. Dexamethasone-loaded ROS-responsive poly(thioketal) nanoparticles suppress inflammation and oxidative stress of acute lung injury. *Bioact Mater*. 2022;14:430–442. doi:10.1016/j.bioactmat.2022.01.047
19. Huppert LA, Matthay MA, Ware LB. Pathogenesis of Acute Respiratory Distress Syndrome. *Semin Respir Crit Care Med*. 2019;40:31–39. doi:10.1053/s-0039-1683996
20. Beitler JR. Lung protection in acute respiratory distress syndrome: what should we target? *Curr Opin Crit Care*. 2020;26(1):26–34. doi:10.1097/MCC.0000000000000692
21. Guan Q, Zhang G, Sun S, et al. Enhanced Oral Bioavailability of Pueraria Flavones by a Novel Solid Self-microemulsifying Drug Delivery System (SMEDDS) Dropping Pills. *Biol Pharm Bull*. 2016;39(5):762–769. doi:10.1248/bpb.b15-00854
22. Stocker R, Yamamoto Y, McDonagh AF, et al. Bilirubin is an antioxidant of possible physiological importance. *Science*. 1987;235(4792):1043–1046. doi:10.1126/science.3029864
23. Kim MJ, Lee Y, Jon S, et al. PEGylated bilirubin nanoparticle as an anti-oxidative and anti-inflammatory demulcent in pancreatic islet xenotransplantation. *Biomaterials*. 2017;133:242–252. doi:10.1016/j.biomaterials.2017.04.029
24. Calfee CS, Delucchi KL, Sinha P, et al. Acute respiratory distress syndrome subphenotypes and differential response to simvastatin: secondary analysis of a randomised controlled trial. *Lancet Respir Med*. 2018;6(9):691–698. doi:10.1016/S2213-2600(18)30177-2
25. Horsfall LJ, Rait G, Walters K, et al. Serum bilirubin and risk of respiratory disease and death. *JAMA*. 2011;305:691–697. doi:10.1001/jama.2011.124
26. Ji HL, Zhao R, Matalon S, et al. Elevated Plasmin(ogen) as a Common Risk Factor for COVID-19 Susceptibility. *Physiol Rev*. 2020;100:1065–1075. doi:10.1152/physrev.00013.2020
27. Wali M, Zhu JQ, Zhai ZH, et al. ROS-responsive polymer nanoparticles with enhanced loading of dexamethasone effectively modulate the lung injury microenvironment. *Acta Biomater*. 2022;148:258–270. doi:10.1016/j.actbio.2022.06.024
28. Domscheit H, Hegeman MA, Carvalho N, et al. Molecular Dynamics of Lipopolysaccharide-Induced Lung Injury in Rodents. *Front Physiol*. 2020;11:1–8. doi:10.3389/fphys.2020.00036
29. Matute-Bello G, Downey G, Moore BB, et al. An official American Thoracic Society workshop report: features and measurements of experimental acute lung injury in animals. *Am J Respir Cell Mol Biol*. 2011;44:725–738. doi:10.1165/rcmb.2009-0210ST

30. Lu F, Wu SH, Hung Y, et al. Size effect on cell uptake in well-suspended, uniform mesoporous silica nanoparticles. *Small*. 2009;5:1408–1413. doi:10.1002/sml.200900005
31. Su SH, Xu AH, Chen Y, et al. Transcriptomic Analysis of Pulmonary Microvascular Endothelial Cells with IQGAP1 Knockdown. *DNA Cell Biol*. 2020;39(7):1127–1140. doi:10.1089/dna.2020.5451
32. Su S, Xu A, Chen Y, et al. Transcriptomic Analysis of Pulmonary Microvascular Endothelial Cells with IQGAP1 Knockdown. *DNA Cell Biol*. 2020;39(7):1127–1140.
33. Ding P, Yang R, Li C, et al. Fibroblast growth factor 21 attenuates ventilator-induced lung injury by inhibiting the NLRP3/caspase-1/GSDMD pyroptotic pathway. *Crit Care*. 2023;27(1):196–211. doi:10.1186/s13054-023-04488-5
34. Tang S, Jiang J, Zhang N, et al. Tumor necrosis factor- $\alpha$  requires Ezrin to regulate the cytoskeleton and cause pulmonary microvascular endothelial barrier damage. *Microvasc Res*. 2021;133:104093. doi:10.1016/j.mvr.2020.104093
35. Zhou Z, He H, Wang K, et al. Granzyme A from cytotoxic lymphocytes cleaves GSDMB to trigger pyroptosis in target cells. *Science*. 2020;368(6494):eaaz7548. doi:10.1126/science.aaz7548
36. Shao F. Gasdermins: making pores for pyroptosis. *Nat Rev Immunol*. 2021;21(10):620–621. doi:10.1038/s41577-021-00602-2
37. Lee IT, Yang CM. Role of NADPH oxidase/ROS in pro-inflammatory mediators-induced airway and pulmonary diseases. *Biochem Pharmacol*. 2012;84(5):581–590. doi:10.1016/j.bcp.2012.05.005
38. Herzberger J, Fischer K, Leibig D, et al. Oxidation-Responsive and “Clickable” Poly(ethylene glycol) via Copolymerization of 2-(Methylthio)ethyl Glycidyl Ether. *J Am Chem Soc*. 2016;138:9212–9223. doi:10.1021/jacs.6b04548
39. Yusheng Z, Yue Z, Hui K, et al. Protective Effects of Carbon Dots Derived from Armeniaceae Semen Amarum Carbonisata Against Acute Lung Injury Induced by Lipopolysaccharides in Rats. *Int J Nanomed*. 2022;17:1–14. doi:10.2147/IJN.S338886
40. Zhenhao L, Haitao P, Jihong Y, et al. Xuanfei Baidu formula alleviates impaired mitochondrial dynamics and activated NLRP3 inflammasome by repressing NF- $\kappa$ B and MAPK pathways in LPS-induced ALI and inflammation models. *Phytomedicine*. 2023;108:154545. doi:10.1016/j.phymed.2022.154545
41. Sena LA, Chandel NS. Physiological roles of mitochondrial reactive oxygen species. *Mol Cell*. 2012;48(2):158–167. doi:10.1016/j.molcel.2012.09.025
42. Brieger K, Schiavone S, Miller FJ, et al. Reactive oxygen species: from health to disease. *Swiss Med Wkly*. 2012;142:w13659. doi:10.4414/smw.2012.13659
43. Giordo R, Nasrallah GK, Al-Jamal O, et al. Resveratrol Inhibits Oxidative Stress and Prevents Mitochondrial Damage Induced by Zinc Oxide Nanoparticles in Zebrafish (Danio rerio). *Int J Mol Sci*. 2020;21(11):3838. doi:10.3390/ijms21113838
44. Phosri S, Jangpromma N, Patramanon R, et al. Protective Effect of Crocodile Hemoglobin and Whole Blood Against Hydrogen Peroxide-Induced Oxidative Damage in Human Lung Fibroblasts (MRC-5) and Inflammation in Mice. *Inflammation*. 2017;40(1):205–220. doi:10.1007/s10753-016-0471-7
45. Jin F, Liu D, Yu H, et al. Sialic Acid-Functionalized PEG-PLGA Microspheres Loading Mitochondrial-Targeting-Modified Curcumin for Acute Lung Injury Therapy. *Mol Pharm*. 2019;16(1):71–85. doi:10.1021/acs.molpharmaceut.8b00861
46. Wang M, Wang K, Deng G, et al. Mitochondria-Modulating Porous Se@SiO<sub>2</sub> Nanoparticles Provide Resistance to Oxidative Injury in Airway Epithelial Cells: implications for Acute Lung Injury. *Int J Nanomed*. 2020;15:2287–2302. doi:10.2147/IJN.S240301
47. Kim JY, Lee DY, Kang S, et al. Bilirubin nanoparticle preconditioning protects against hepatic ischemia-reperfusion injury. *Biomaterials*. 2017;133:1–10. doi:10.1016/j.biomaterials.2017.04.011
48. Lee Y, Sugihara K, Gilliland MG, et al. Hyaluronic acid-bilirubin nanomedicine for targeted modulation of dysregulated intestinal barrier, microbiome and immune responses in colitis. *Nat Mater*. 2020;19(1):118–126. doi:10.1038/s41563-019-0462-9
49. Yu H, Jin F, Liu D, et al. ROS-responsive nano-drug delivery system combining mitochondria-targeting ceria nanoparticles with atorvastatin for acute kidney injury. *Theranostics*. 2020;10(5):2342–2357. doi:10.7150/thno.40395
50. Anselmo AC, Gupta V, Zern BJ, et al. Delivering nanoparticles to lungs while avoiding liver and spleen through adsorption on red blood cells. *ACS Nano*. 2013;7(12):11129–11137. doi:10.1021/nn404853z
51. Gotts JE, Abbott J, Matthay MA. Influenza causes prolonged disruption of the alveolar-capillary barrier in mice unresponsive to mesenchymal stem cell therapy. *Am J Physiol Lung Cell Mol Physiol*. 2014;307(5):L395–406. doi:10.1152/ajplung.00110.2014
52. Fang CL, Wen CJ, Aljuffali IA, et al. Passive targeting of phosphatidylserine increases ropivacaine delivery to the lungs for treatment of acute lung injury: an animal study. *J Control Release*. 2015;213:69–78. doi:10.1016/j.jconrel.2015.06.038
53. Yingjun L, Dongdong S, Qin F, et al. The enhanced permeability and retention effect based nanomedicine at the site of injury. *Nano Res*. 2020;13:564–569. doi:10.1007/s12274-020-2655-6
54. Ma B, Xu H, Zhuang W, et al. Reactive Oxygen Species Responsive Theranostic Nanoplatfor for Two-Photon Aggregation-Induced Emission Imaging and Therapy of Acute and Chronic Inflammation. *ACS Nano*. 2020;14(5):5862–5873. doi:10.1021/acsnano.0c01012
55. Jiang R, Zhao S, Wang R, et al. Safety and Efficacy of Atorvastatin for Chronic Subdural Hematoma in Chinese Patients: a Randomized Clinical Trial. *JAMA Neurol*. 2018;75(11):1338–1346. doi:10.1001/jamaneurol.2018.2030